FeN$_4$-doped carbon nanotubes derived from metal organic frameworks for effective degradation of organic dyes by peroxymonosulfate: Impacts of FeN$_4$ spin states

Meng Li [a,d,1], Zilong Li [a,1], Xiaolong Yu [b], Yinlong Wu [a], Cehui Mo [a], Mi Luo [c], Ligui Li [c,*], Shaoqi Zhou [d], Qiming Liu [e], Nan Wang [a,*], King Lun Yeung [f], Shaowei Chen [e,*]

[a] *Guangdong Provincial Research Center for Environment Pollution Control and Remediation Materials, College of Life Science and Technology; Guangdong Provincial Key Laboratory of Optical Fiber Sensing and Communications, Siyuan laboratory, Guangzhou Key Laboratory of Vacuum Coating Technologies and New Energy Materials, Guangdong Provincial Engineering Technology Research Center of Vacuum Coating Technologies and New Energy Materials, Department of Physics, Jinan University, Guangzhou, Guangdong 510632, PR China*

[b] *Guangdong Provincial Key Laboratory of Petrochemical Pollution Processes and Control, School of Environmental Science and Engineering, Guangdong University of Petrochemical Technology, Maoming, Guangdong 525000, PR China*

[c] *Guangzhou Key Laboratory for Surface Chemistry of Energy Materials, New Energy Research Institute, School of Environment and Energy, South China University of Technology, Guangzhou 510006, PR China*

[d] *College of Resources and Environmental Engineering, Guizhou University, 2708 Huaxi Road, Guiyang 550025, PR China*

[e] *Department of Chemistry and Biochemistry, University of California, 1156 High Street, Santa Cruz, CA 95064, USA*

[f] *Department of Chemical and Biological Engineering, The Hong Kong University of Science and Technology, Clear Water Bay, Kowloon, Hong Kong SAR, PR China*

ARTICLE INFO

ABSTRACT

Development of low-cost, high-performance catalysts for the effective degradation of organic dyes is of both fundamental and technological significance for environmental remediation. Herein, FeN$_4$-doped carbon nanotubes exhibit a remarkable catalytic activity towards the degradation of acid orange 7 (AO7) in the presence of peroxymonosulfate (PMS). This is accounted for by the abundant well-dispersed FeN$_4$ sites and appropriate adsorption energy. Radical quenching experiments and electron paramagnetic resonance measurements suggest that singlet oxygen is the main reactive oxygen species. ^{57}Fe Mossbauer spectroscopy measurements show that the FeN$_4$ moieties contain multiple spin states, and in conjunction with density functional theory calculations, confirm that FeN$_4$ with a low/medium spin state serves as the key sites for PMS activation and hence AO7 degradation. Results from this study highlight the critical role of spin states in FeN$_4$ in the generation of singlet oxygen for effective degradation of organic pollutants.

1. Introduction

The accumulation of hazardous and toxic contaminants, such as pesticides, antibiotics [1], dyes [2], and endocrine disruptors [3], in surface water and groundwater has caused severe environmental pollution issues. Various technologies, such as biological degradation [4], physical adsorption [5], membrane filtration [6], electro-Fenton [7], and advanced oxidation processes (AOPs) [8], have been explored to remove organic pollutants from the environment. Among these, AOPs have shown a high efficiency in removing organic contaminants from water due to the generation of highly reactive species [9]. In fact,
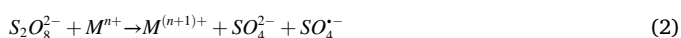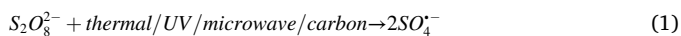
sulfate-based AOPs have received extensive attention in the degradation of organic pollutants, due to strong oxidation ability, wide pH range, low cost, and high stability [10,11]. In this process, sulfate radicals ($SO_4^{\bullet-}$) can be generated by the activation of peroxydisulfate (PDS) and peroxymonosulfate (PMS) by thermal control [12], transition metals [13], UV [14], microwave irradiation [15], etc, as manifested in eqs. (1, 2), and responsible for the oxidative degradation of organic pollutants. Nevertheless, the application of such processes is generally limited due to the high cost and energy input, non-ideal activation performance, and release of metal ions that may lead to secondary pollution [17-20]. Consequently, development of metal-free heterogeneous catalysts for

---

* Corresponding authors.
E-mail addresses: esguili@scut.edu.cn (L. Li), nanwang@jnu.edu.cn (N. Wang), shaowei@ucsc.edu (S. Chen).
[1] These authors contributed equally.

PMS activation is urgently needed.

$$S_2O_8^{2-} + thermal/UV/microwave/carbon \rightarrow 2SO_4^{\bullet-} \quad (1)$$

$$S_2O_8^{2-} + M^{n+} \rightarrow M^{(n+1)+} + SO_4^{2-} + SO_4^{\bullet-} \quad (2)$$

Over the past few years, metal-free carbon-based materials have been used as PMS activators for the degradation of organics pollutants [21], such as carbon nanotubes (CNT) [22], activated carbon (AC) [23], graphene oxide (GO) [24], and nanocarbons [25]. Yet, the catalytic performance has remained subpar as compared to those of the metal-based counterparts. Also, whereas a good removal efficiency can be achieved by the addition of a large amount of oxidants [26], the accumulation of excessive sulfate ions may lead to corrosion of the pipeline in the drinking water and sewer systems [27]. Moreover, the stability and reusability of carbon-based materials is usually poor, limiting their practical applications. Consequently, it is important to develop metal-free PMS catalysts with excellent high catalytic activity and reusability. Recently, numerous studies have been carried out to enhance the catalytic activity of carbon-based materials by the incorporations of heteroatom into the carbon frameworks, such as nitrogen, sulfur, phosphorus, and boron [28-30], wherein heteroatom-doping is recognized as an effective method by regulating the charge distribution of the sp^2-hybridized carbon frameworks and providing abundant active sites for catalysis [31]. For example, nitrogen-doped single-walled carbon nanotubes can significantly improve the catalytic activity for phenol degradation by activating PMS up to 57 times that of pristine carbon nanotubes [32]. Nevertheless, the catalytic activity of metal-free catalysts is usually suppressed via a non-radical process. This can be mitigated by further structural engineering such that practical application is feasible.

One strategy is to embed transition metal-nitrogen coordination centers within a porous carbon scaffold [33]. The resulting metal-nitrogen-carbon (M−N−C, M = Mn, Co, Fe, Ni, etc.) catalysts possess a high density of active sites and exhibit promising catalytic activity in various reaction processes [34-36]. Of these, the nitrogen-coordinated iron (FeN$_x$) moieties are of particular interest [37], which can impact the electronic structure of the catalyst surface and electrical conductivity. Both factors are conducive to PMS activation [38], which is believed to follow three reaction pathways, i.e., radicals, singlet oxygen, and direct electron transfer [39]. Of these, singlet oxygen ($^1O_2$) is known to exhibit high selectivity and mild redox ability (2.2 V) for the degradation of organic contaminants, in comparison with other radical species, such as $^{\bullet}OH$ (2.7 V) and $SO_4^{\bullet-}$ (2.5–3.1 V) [40].

These Fe-N-C catalysts are usually prepared by fixing Fe atoms within a porous support, e.g., graphene oxide (GO), activated carbon (AC), and covalent organic frameworks [41]. Yet the preparation generally entails a complex process, producing a large and uncontrollable structure [42]. Metal-organic frameworks (MOFs), a class of porous crystalline materials, represent an effective alternative. MOFs are constructed by the self-assembly of transition metals and organic ligands [43], and have been extensively explored for various applications, such as molecular sensing, catalysis, pollutant adsorption, and gas separation, due to their excellent conductivity, high catalytic activity, good absorbability, and large surface area [44]. In addition, MOFs can serve as self-sacrificial templates or precursors to synthesize carbon composites based on the unique structure of metal clusters and ligands [45]. For instance, Zn-based MOF (ZIF-8) with a cavity structure can incorporate Fe-containing salts for the preparation of FeN$_x$-doped carbon composites [46]. As the Zn species in ZIF-8 can be evaporated at elevated temperatures, a porous carbon skeleton is formed with a large surface area [39], where the Fe species are typically in form of FeN$_x$ and/or Fe nanoparticles (NPs) [47]. Note that the former is catalytically active whereas the latter inactive in PMS activation [48]. In most prior studies, Fe(NO$_3$)$_3$, FeSO$_4$ and FeCl$_3$ have been commonly used as the Fe precursors, where Fe(OH)$_3$ is generally produced at high temperatures increasing

the amount of Fe NPs [49], and the number of active FeN$_x$ species is in general limited by controlled pyrolysis of these Fe salt precursors [50].

In recent years, functional composites of M−N−C composites have been confirmed as an effective catalysts to activate persulfate [51-53], and the MN$_x$ coordination moieties are found to be responsible for PMS activation and contaminant degradation [50,54]. For instance, Li et al. reported that high-performance Fenton-like Fe-N-C derived from Fe-doped zeolitic imidazolate framework showed a significantly enhanced performance in the degradation of BPA, as compared to Fe nanoparticles-loaded N-doped carbon [50]. Note that the FeN$_x$ moieties can regulate the electronic structures and electrical conductivity of the nanocomposite for the effective activation of PMS [47,55]. However, studies have been scarce focusing on the impact of the FeN$_x$ spin state on the catalytic performance, which are known to influence the adsorption of reactants and key intermediates. This is the primary motivation of the present study.

Herein, FeN$_4$-doped carbon nanotubes are derived from MIL-101 by ball milling and pyrolysis and exhibit an effective performance in the activation of PMS for the degradation of organic dyes. The obtained catalysts retain the original morphology of ZIF-8 with a high surface area and abundant internal channels. In addition, due to the space confinement effect, FeN$_4$ sites are effectively isolated within the carbon framework, and no Fe NPs are formed. The resulting FeNC nanocomposites exhibit apparent catalytic activity in the activation of PMS and the degradation of a range of organic dyes, such as acid orange 7 (AO7), methyl red (MR), rhodamine B (RhB), acid orange G (AOG), and methyl orange (MG). Radical quenching experiments and electron paramagnetic resonance (EPR) spectroscopy measurements show that singlet oxygen is the reactive oxidative species (ROS) responsible for the catalytic activity. In conjunction with DFT calculations, medium- and low-spin FeN$_4$ is identified as the most active species that facilitate the adsorption and activation of PMS and ultimately the degradation of organic pollutants. Furthermore, the degradation mechanism and pathway are proposed based on the identification of key reaction intermediates by gas chromatography-mass spectrometry and Fukui index which suggests the atomic sites within the dye molecules for radical attacks.

2. Experimental section

2.1. Materials

Ferric chloride hexahydrate (FeCl$_3$·6H$_2$O, 99.5%), zinc nitrate hexahydrate (Zn(NO$_3$)$_2$·6H$_2$O, 99.5%), *p*-phthalic acid, dimethylformamide (DMF), ethanol (EtOH), methanol (MeOH), *tert*-butanol (TBA), 5,5-dimethyl-1-pyrroline N-oxide (DMPO), and 2,2,6,6-tetramethyl-4-piperidone (TEMP) were purchased from Aladdin (Shanghai, China). Oxone (2KHSO$_5$•KHSO$_4$•K$_2$SO$_4$), L-histidine, *p*-benzoquinone, AO7, MR, RhB, AOG, and MG were obtained from Sigma-Aldrich (Shanghai, China). All chemicals in this study were used directly without further purification. Water was supplied with a Barnstead Water Purification System (18.2 MΩ cm).

2.2. Synthesis of catalysts

Synthesis of MIL-101
MIL-101 was prepared by following a literature procedure [56]. In brief, 1.71 g of FeCl$_3$·6H$_2$O and 0.41 g of *p*-phthalic acid were added into 30 mL of DMF under stirring for 30 min, and the resulting mixture was heated in a hydrothermal reactor at 110 °C for 20 h. The precipitate was rinsed several times with ethanol, DMF and deionized water, and dried in a vacuum oven at 70 °C overnight.
Synthesis of ZIF-8
ZIF-8 was prepared by using the traditional solution method [57]. Experimentally, 1.68 g of Zn(NO$_3$)$_2$·6H$_2$O was dispersed into 20 mL of MeOH, which was then combined with a 60 mL MeOH solution

containing 4 g of dimethylimidazole under magnetic stirring. The solution turned milky white, and was let to stand overnight at room temperature. The bottom product was collected by centrifugation, rinsed with distilled water and absolute ethanol, and then dried under vacuum at 70 °C overnight.

Synthesis of FeN_4-doped carbon nanotubes

The two precursors of MIL-101 and ZIF-8 obtained above were mixed and ground by ball milling under the protection of a N_2 atmosphere at different mass ratios (1:15, 1:20, and 1:25), and the powders were placed in a tube furnace and heated at 900 °C under a N_2 atmosphere for 2 h, affording FeN_4-doped carbon nanotubes, which were denoted as FeNC-15, FeNC-20, and FeNC-25, respectively. The samples were then subject to a second heating treatment in an NH_3 atmosphere at 950 °C for half an hour to increase the amount of N doping. Preparation of Fe-Nx-fer catalyst, FeNC-fer uses the same preparation method as FeNC-20 but uses ferrocene or $FeCl_3 \cdot H_2O$ instead of MIL-101 for the iron precursor.

2.3. Characterization

Transmission electron microscopic (TEM) measurements were conducted on a Tecnai G2-F20 equipped with an energy-dispersive X-ray spectroscopy (EDS) detector at the acceleration voltage of 100 kV. The TEM samples were prepared by dropcasting a catalyst dispersion onto a copper grid coated with a holy carbon film. The morphology and structure of the samples were studied by scanning electron microscopy (SEM, Gemini FE-SEM). Powder X-ray diffraction (XRD) patterns were recorded with a Rigaku-D/Max-IIIA diffractometer using Cu K_α radiation. X-ray photoelectron spectroscopy (XPS) experiments were carried out on a Thermo-ESCA-Lab 250 instrument with Al $K\alpha$ radiation. The Brunauer-Emmett-Teller (BET) surface area was determined by using a Kubo-X1000 instrument at 77 K. Raman spectra were recorded on a RENISHAW inVia instrument with an Ar laser source of 488 nm in a macroscopic configuration. Inductively coupled plasma atomic emission spectrometric (ICP-AES) measurements were carried out with a Liberty-ax instrument. The X-ray absorption spectroscopys (XAS) measurements and standard contrast samples used were provided by Taiwan Light Source.

2.4. Catalytic degradation experiment

The catalytic degradation experiments were carried out in a 300 mL flat bottom breaker at ambient temperature at a stirring speed of 350 rpm. The degradation reaction was initiated by adding a calculated amount of PMS and FeNC catalysts into the dye solution. The solution pH was adjusted by NaOH (10 mM) and H_2SO_4 (10 mM). An adsorption equilibrium between the catalysts and target contaminants was achieved by stirring the mixture for 30 min. During the catalytic reaction, 1 mL of the sample solution was taken out at certain time points, and filtered with a 0.25 μm polytetrafluoroethylene (PTFE) Millipore membrane, before the optical absorbance was quantified. To test the durability and stability of the catalysts, the catalyst samples were collected by centrifugation from the reaction vessel, rinsed with deionized water, and used for repeated dye degradation. In the degradation process of AO7, the corresponding Total Organic Carbon (TOC) was measured by a TOC analyzer (Shimadzu, Kyoto, Japan) at certain time intervals. The reaction conditions included the dye concentration of 50 mg L^{-1}, catalyst concentration of 2 mg L^{-1}, PMS concentration of 0.5 mM, and solution pH = 7.

2.5. Analysis

The dye concentration was determined via the spectrophotometric method on a Shimadzu U2800 UV–vis spectrophotometer. For MR, RhB, AOG, MG, and AO7, their maximum adsorption wavelengths are 527, 553, 476, 464, and 484 nm, respectively. EPR measurements were

conducted on a Bruker A300 spectrometer with TEMP and DMPO as the spin-trapping agents. The degradation dynamics of AO7 was fitted with a pseudo-first-order kinetic equation, $\ln C/C_0 = -kt$, where k was the reaction rate, t was the reaction time, and C and C_0 were the concentration of AO7 at time t and 0, respectively [58-60].

The degradation products of AO7 were determined by gas chromatography-mass spectrometry (GC–MS, 7890A-5975C, Agilent, USA) equipped with an HP-5MS capillary column (30.0 m × 250 μm × 0.25 μm, Shimadzu, Japan). High-purity helium was utilized as the carrier gas at the rate of 1 mL min^{-1}. The column temperature was initially set at 60 °C and held for 5 min, then raised to 280 °C at a rate of 10 °C min^{-1} and held for 10 min, next to 260 °C, finally to 280 °C. The MS analysis was carried out in the EI mode (70 eV), and ion source and quadrupole temperatures were set at 200 and 150 °C, respectively. The scanning mass range was 35 to 500 m/z, and the corresponding degradation products were identified utilizing the MS database and NIST11 search as references.

2.6. Computational methods

The molecular orbital analysis was carried out by utilizing the Gaussian 09 program [61], and the optimized structural geometry with the minimum energy was conducted at the b3lyp/6–31 g* level. The lowest unoccupied molecular orbital (LUMO) and the highest occupied molecular orbital (HOMO) were obtained from the output files of Gaussian 09. The Fukui function values of electrophilic reaction (*f*) were calculated based on the charge distribution from Multiwfn 3.7 [62].

DFT calculations were performed with the CASTEP code of the Materials Studio package of Acclerys Inc. In all calculations, the generalized gradient approximation and the projector augments wave pseudopotentials with the exchange and correlation in the Perdew–Burke–Ernzerhof were employed. The plane-wave cutoff energy was set at 450 eV. The convergence of forces and energy on each atom during structure relaxation were set to 0.03 eV $Å^{-1}$ in force and 10^{-6} eV in energy, respectively. The Brillouin zone was sampled with a 3 × 3 × 1 Monkhorst-Pack k-point grid. The optimized structure sizes for pyrrolic, graphitic, pyridinic and FeN_4 were 12.26 × 12.26 × 15 Å, and Fe_2O_3(0 0 1) and Fe(1 1 0) were 10.07 × 10.07 × 20 Å and 9.49 × 9.49 × 20 Å, respectively. The vacuum space along the z[1] direction was more than 15 Å, to avoid interplanar interactions. For geometric optimization of the slab models, the top two layers were allowed to relax. Van der Waals (vdW) interaction was taken into account at the DFT-D_3 level as proposed by Grimme. The adsorption energy was defined as $E_{ads} = E_{total} - (E_{substrates} + E_{PMS})$, where E_{total}, $E_{substrates}$, and E_{PMS} denote the total energy of substrates with PMS, substrates, and PMS, respectively.

3. Results and discussion

3.1. Structural characterization

As shown in Fig. 1, the FeNC nanocomposites were prepared by ball milling of two precursors of ZIF-8 and MIL-101 followed by controlled pyrolysis of the mixture. ZIF-8 is a rhombic dodecahedron framework with a large specific surface area (crystal size 2 nm), and MIL-101 is a rhombic crystal framework containing unique monodisperse Fe centers and carboxylic acid bridge ligands (crystal particles about 30 nm in size, Figure S1). Their XRD patterns are consistent with those reported in the literature [63] (Figure S2). Ball milling helped create uniform mixing of the elements (i.e., C, N, Fe, etc.) in the sample, and pyrolysis facilitated the formation of a carbon skeleton with a tubular structure, which exhibited a large specific surface area, and contained abundant FeN_4 moieties. Furthermore, the second heat treatment in an ammonia atmosphere effectively increased the contents of Fe-N and C-N bonds, and the microporosity of the samples.

The crystalline structure of FeNC-20 was then characterized by XRD measurements. From Figure S2a, one can see that the FeNC samples all
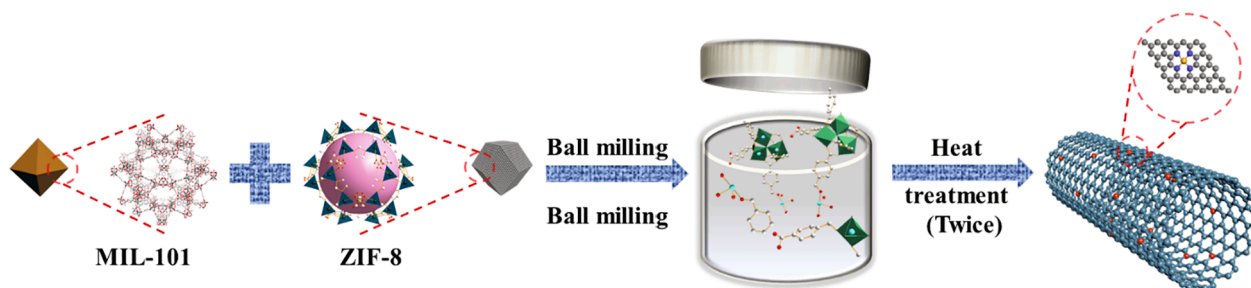
Fig. 1. Schematic illustration of the preparation of FeN$_4$-doped nanotubes.

exhibited only two intense diffraction peaks at $2\theta = 26°$, which can be indexed to the (0 0 2) lattice planes of graphite carbon (PDF#75–1621), indicating successful transformation of the MOF precursors to graphitized carbon. The additional diffraction peak at $2\theta = 44°$ likely arose from metal nanoparticles of iron (PDF#89–7194) or Fe$_X$C (PDF#52–0512), which is consistent with the results of TEM measurements (Fig. 2). The pyrolytic product of MIL-101 exhibited similar XRD patterns, whereas only a carbon diffraction peak was observed for ZIF-8 after pyrolysis (Figure S3).

The structures of the obtained nanocomposites were first examined by TEM measurements. From Fig. 2a, 2b and 2d, FeNC-20 can be seen to exhibit a porous network of CNTs with a bamboo-like structure featuring a tube diameter of about 100 nm and shell thickness of ca. 6 nm. From the high-resolution TEM image in Fig. 2c, one can see that FeNC-20 displayed well-defined lattice fringes, with an interplanar spacing of ca. 0.40 nm that is consistent with the (0 0 2) crystal planes of graphitic

carbon (card #75–1621). Similar structures were observed for FeNC-15 and FeNC-25 (Figure S4). Note that a small number of dark-contrast nanoparticles can also be identified in the TEM image of FeNC-20 (Fig. 2e); and elemental mapping analysis (Fig. 2f-2i) suggest that these are most likely Fe or Fe$_3$C nanoparticles, embedded within a N-doped carbon matrix. Additionally, isolated Fe can be seen to be distributed rather uniformly across the sample, along with C and N, suggesting the formation of FeNx moieties within the carbon nanotubes.

The nanotubular structure is also evident in SEM measurements (Figure S5). For the samples prepared at either higher or lower Fe feed (i. e., FeNC-15 and FeNC-25), the fraction of nanotubes was markedly lower, and the samples consisted mostly of irregular aggregates. This led to a reduced specific surface area and likely compromised the accessibility of the active sites and hence the catalytic activity (vide infra). In addition, the SEM image of ZIF-8, ZIF-8–900, MIL-101, and MIL-101–900 (Figure S6a-6d) confirm that ball milling can facilitate the
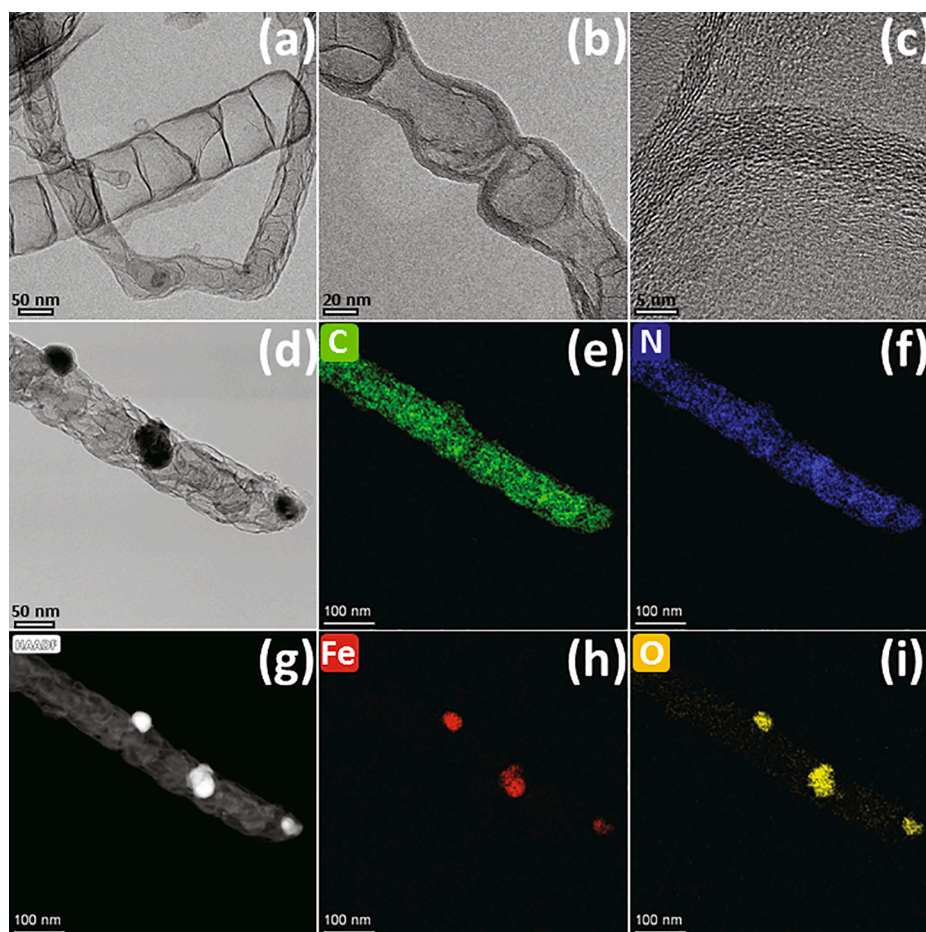

Fig. 2. (a-d) Representative TEM images and (e-i) EDS elemental maps of FeNC-20.

formation of the nanotubes. As is shown in Figure S7, the SEM images of FeNC-fer (uses ferrocene or $FeCl_3 \cdot H_2O$ as precursor) reveal the advantages of MIL-101 as an iron source for the formation of carbon nanotube structures.

From the nitrogen adsorption–desorption isotherms (Figure S8a-8b), FeNC-20 can be seen to show an obvious H_4 hysteresis loop, indicating the formation of micropores and mesopores in the sample (Figure S8b) [64], with a specific surface area of 926.3 $m^2 g^{-1}$, more than twice those of other samples in the series (inset to Figure S8a). The abundant micropores in FeNC-20 are anticipated to facilitate access to the active sites [28,65]; and mesopores are known to be advantageous for mass transfer of reactants and products (Figure S8c-8d).

Further structural insights were obtained in Raman spectroscopic measurements. From Figure S9, the three FeNC samples can be seen to display two vibrational bands at approximately 1350 and 1595 cm^{-1}, due to the structural defects in the graphitic structure (D band) and graphitic sp^2 C (G band), respectively [66], with an intensity ratio (I_D/I_G) of 1.196, 1.20, and 1.197 for FeNC-15, FeNC-20, and FeNC-25, respectively. This indicates a similar defective structure among the series of samples (slightly more defective with FeNC-20 than the other two).

In ^{57}Fe Mössbauer spectroscopy measurements (Fig. 3a-3c), FeNC-20 was found to contain two components, FeN_4 and Fe/Fe_3C, at different spin states: D_1 ($Fe^{II}N_4$, low spin), D_2 ($Fe^{II}N_4$, medium spin, like FePc), D_3 ($N-Fe^{II}N_{2+2}$, high spin) and α-iron or iron carbide [67]. Note that the quadrupole doublet of D_2–FeN_4 with an isomer shift (IS) of 0.27 mm s^{-1} has been identified to be the main source of activity for heat-treated porphyrins [67,68]. The fact that only a sextet, but no obvious singlet, was observed in the Mössbauer spectra suggests that the content of the superparamagnetic iron was relatively low in the catalyst. That is, the FeNC samples were composed primarily of FeN_4 moieties and only a small amount of α-Fe or iron carbide [67,69], as manifested in TEM measurements (Fig. 2).

Furthermore, in conjunction with ICP-AES measurements, the fractions of the Fe species in different spin states (Fig. 3d and Table S1) were quantitatively assessed. From Fig. 3e, one can see that FeNC-20 primarily contained low-spin FeN_4 (D_1, 0.641 at%) and medium-spin FeN_4 (D_2, 0.223 at%), which are markedly lower in FeNC-15 (0.218, 0.195 at%) and FeNC-25 (0.479 and 0.131 at%). In addition, in the latter two samples, there is a substantial amount of α-Fe or Fe_XC (0.321 and 0.501 at%), respectively.

The elemental composition and valence state of the samples were then evaluated by XPS measurements. From the survey spectra (Figure S10), the elements of C, N, O, and Fe can be readily identified at 284.8, 399.8, 531.5, 712.2 eV, respectively, consistent with the incorporation of Fe and N into the carbon matrix; and from the integrated peak areas, the elemental compositions were estimated and listed in Table S2. One can see that the series of FeNC samples exhibited rather consistent elemental compositions, and FeNC-20 contained a slightly higher N (7.10 at%) and Fe (0.84 at%) content than others. In the high-resolution XPS spectra of the N 1 s electrons (Fig. 3f), deconvolution yields five peaks at 398.4, 399.7, 400.9, 402.0 and 405.1 eV, corresponding to the pyridinic, Fe-Nx, pyrrolic, graphitic and oxidized N (Fig. 3g, Table S3), respectively [28,70-73]. Figure S11a shows the C 1 s spectra of the FeNC series, where sp^2 C represents the dominant species, consistent with the successful graphitization of the MOF precursors by pyrolysis. The Fe 2p spectra was shown in Figure S11b, where the peaks at 708.4, 710.3, 711.9, 714.6 and 718.1 eV were attributed to Fe-N, Fe
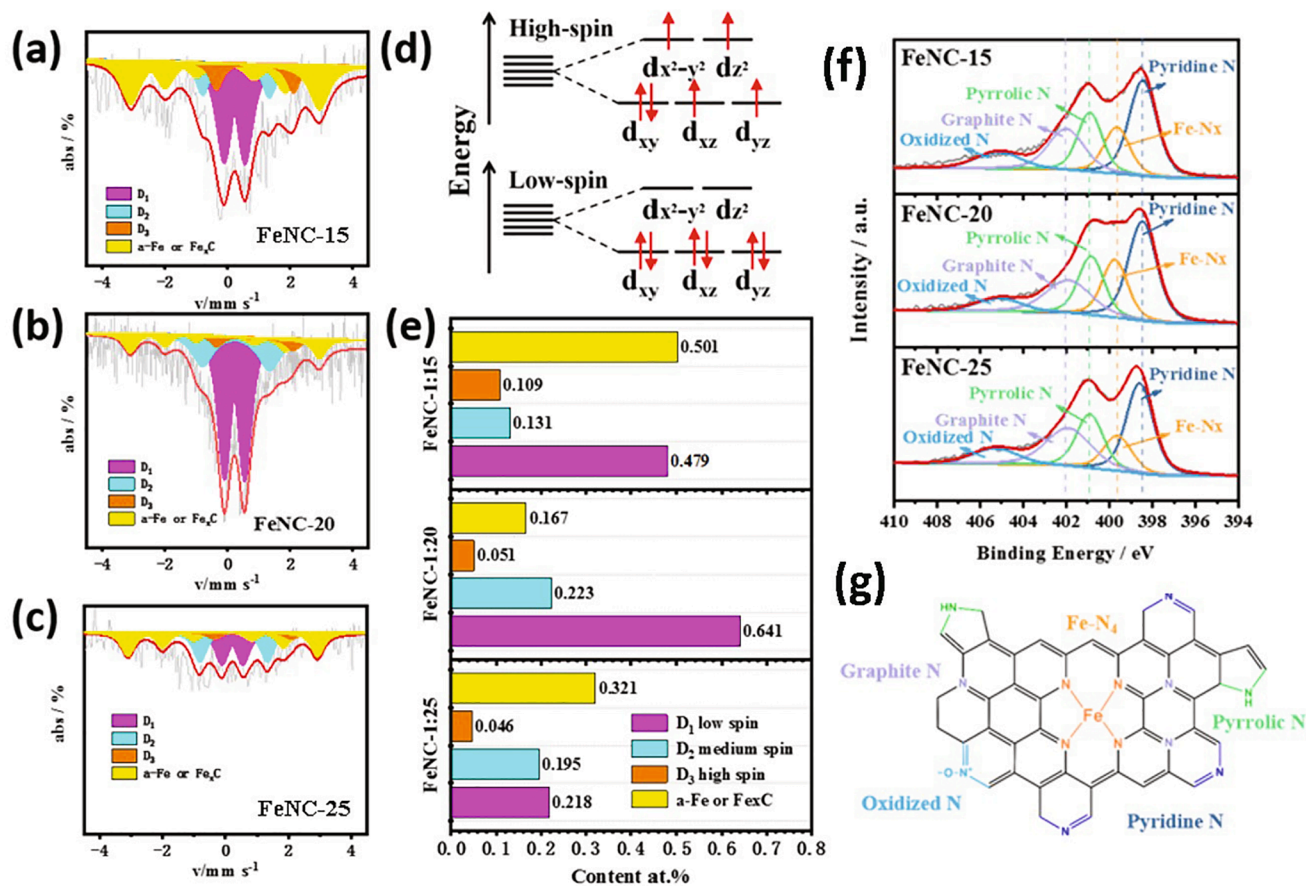

Fig. 3. ^{57}Fe Mössbauer transmission spectra of (a) FeNC-15, (b) FeNC-20, and (c) FeNC-25. (d) Schematic representation of Fe^{2+} in high- and low-spin state, (e) the relative atomic contents of different spin states FeN_4 in the three samples, (f) High-resolution XPS scans of the N 1 s electrons of FeNC-15, FeNC-20, and FeNC-25, and (g) Schematic illustration of the five nitrogen doping configurations in carbon.

(II), satellite of Fe(II), Fe(III), and satellite of Fe(III), respectively [74,75]. In addition, the Fe-N content of the three samples was estimated to be 0.92 at.%, 1.33 at.% and 0.84 at.% (Table S3), respectively. That is, the Fe-N content of the FeNC-20 sample is the highest among the series of samples. This is in good agreement with the results from Mössbauer spectroscopy measurements where FeNC-20 contained the highest concentration of low-/medium-spin species (Fig. 3a-3e).

The electronic structure and coordination configuration of the FeNx moiety in FeNC-20 was then examined by synchrotron-based X-ray absorption spectroscopy (XAS) measurements. Fig. 4a shows the normalized Fe K-edge X-ray absorption near-edge structure (XANES) spectra of FeNC-20 and reference samples. It can be seen that FeNC-20 and FePc displayed a similar absorption edge, white line, and post-edge oscillations, suggesting a rather consistent atomic structure and chemical states of the Fe atoms in the samples. In fact, in the k^3-weighted Fourier transform (Fig. 4b) and wavelet transform (Fig. 4d-f and Figure S12), FeNC-20 exhibits a main peak at 1.58 Å in R space, which is close to that of FePc (1.57 Å). To clearly analyze the coordination structure of the FeNx active site, we first confirmed the range of fitting with the help of k-q comparison (Figure S13). Based on the fitting of the k^2-weighted Fourier transform of the EXAFS data in Fig. 4c, the coordination number (N) of the Fe center was estimated to be about 6, and the bond length between the Fe atom and the four N atoms was ca. 2.0 Å (Table S4, with the misfit, R factor, of only 0.016%). Meanwhile, from the structural model in the inset to Fig. 4c, one can see that there is an additional oxygen atom adsorbed onto the central iron atom with a Fe-O bond length of 1.2 Å. The additional peak at 2.57 Å corresponds to the Fe-Fe bond, indicating that the presence of metallic Fe in the sample.

Interestingly, there is a clear variation of the adsorption energy of PMS onto the different Fe spin structures, as manifested in DFT calculations. Fig. 5a-5i shows the optimal configurations and differential surface charge density of PMS adsorption on $Fe^{II}N_4$ in three different spin structures (D_1-$Fe^{II}N_4$ low spin, D_2-$Fe^{II}N_4$ medium spin, D_3-N-$Fe^{II}N_4$ high spin), in comparison to graphene, Fe_2O_3, Fe, pyridinic N, pyrrolic N, and graphitic N. One can see that medium-spin $Fe^{II}N_4$ exhibits the lowest adsorption energy, followed by low-spin $Fe^{II}N_4$ (Fig. 5j), implying that these two structures are the preferred adsorption sites for PMS. The fact that FeNC-20 possessed the highest contents of low- and medium-spin Fe species among the series of samples (Fig. 3e) suggests that it is

the optimal structure for the catalytic degradation reactions (an additional minor contribution may arise from pyrrolic N which is a close third in PMS adsorption, and FeNC-20 also contained a slightly higher pyrrolic N content than the others, as shown in Table S3).

3.2. Catalytic degradation of organic dyes

Remarkably, the FeNC nanocomposites exhibited apparent catalytic activity in the oxidative degradation of AO7 by PMS. As shown in Fig. 6a, AO7 degradation was negligible in PMS or FeNC-20 alone (the 13.9% loss of AO7 in the presence of FeNC-20 was due to adsorption). In contrast, when both FeNC-20 and PMS were present, 100% of AO7 was degraded within 5 min at the optimal pH of 7 (optimization of catalyst and PMS loadings, as well as solution pH can be found in Figure S14), suggestive of effective activation of PMS by FeNC-20 in the oxidative degradation of AO7. This performance is markedly better than those when ZIF-8 (39.6%) and MIL-101 (71.7%) was used instead for PMS activation. In addition, by fitting the AO7 degradation curves with the pseudo-first-order kinetic model, the reaction rate was estimated, which was the highest at 0.811 min^{-1} for FeNC-20, in comparison to 0.732 min^{-1} for FeNC-25, 0.403 min^{-1} for FeNC-15, 0.226 min^{-1} for MIL-101, and 0.154 min^{-1} for ZIF-8 (Fig. 6a inset), confirming the effectiveness of the low- and medium-spin FeN$_4$ moieties in activating PMS for AO7 degradation. The degradation performance of AO7 by FeNC-fer catalyst with PMS is still passable (Figure S15), which supported the above results.

Notably, the Fe-NC/PMS system was also active in the degradation of other organic dyes, such as MR, RhB, AOG, and MO (Fig. 6b), where the removal was all completed within 5 min. The corresponding reaction rate was estimated to be 0.291, 0.203, 1.726, and 1.094 min^{-1} for MR, RhB, AOG, and MO, respectively (Fig. 6b inset). These results demonstrate that the Fe-N$_4$/PMS combination can be used as an effective catalyst for the degradation of a wide range of organic pollutants in wastewater. Notably, such performances were significantly higher than those of relevant catalysts reported recently in the literature (Table S5).

3.3. Analysis of reactive oxygen species and activation mechanisms

It has been known that AOPs generally involve reactive species, such
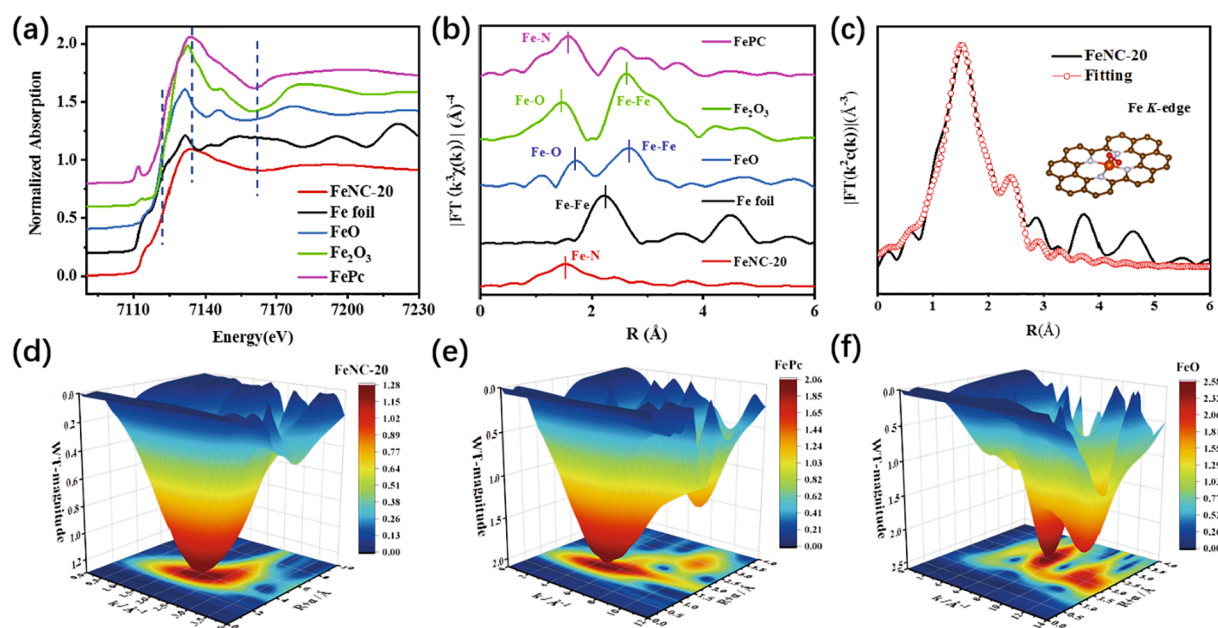

Fig. 4. (a) Fe K-edge XANES spectra and (b) Fourier transforms of the Fe K-edge EXAFS oscillations of FeNC-20 and reference samples (Fe foil, FeO, Fe$_2$O$_3$ and FePc). (c) The corresponding EXAFS fitting result of FeNC-20 in R space (the inset is the coordination structure of FeN(O). (d, e, f) WT-EXAFS of FeNC-20, FePc and Fe foil.
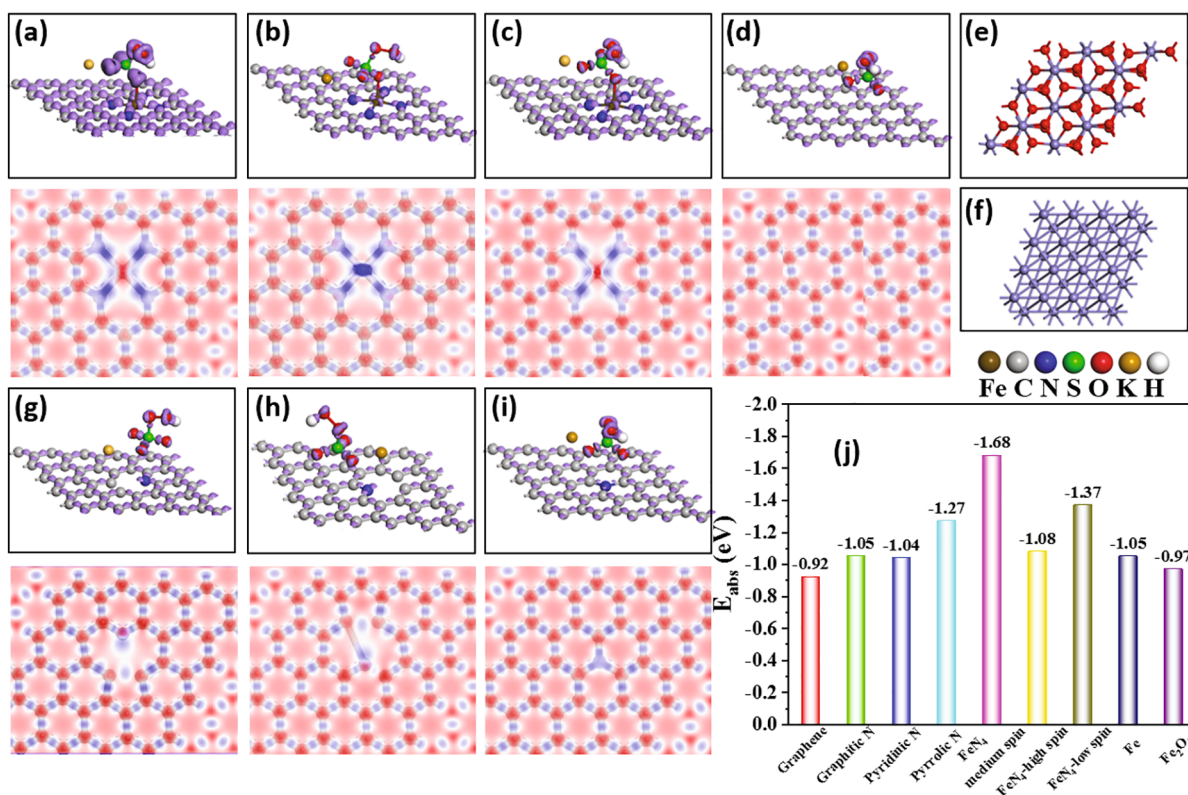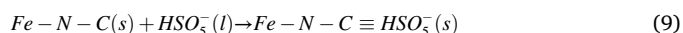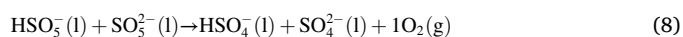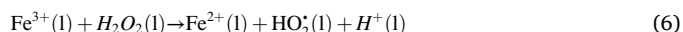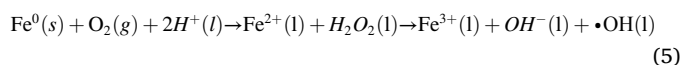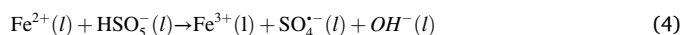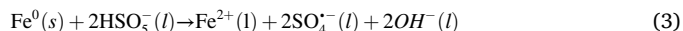
Fig. 5. Optimized configurations (top panels) and differential surface charge density diagrams (bottom panels) of PMS adsorbed on (a) D_1-$Fe^{II}N_4$, low spin, (b) D_2-$Fe^{II}N_4$, medium spin, (c) D_3-N-$Fe^{II}N_4$, high spin, (d) carbon, (e) Fe_2O_3, (f) Fe, (g) pyridinic N, (h) pyrrolic N, and (i) graphitic N. (j) Adsorption energy of PMS onto different carbon configurations. For the Fe-containing samples, the adsorption site is the Fe center, whereas for the metal-free samples, it is the C adjacent.

as $SO_4^{\bullet-}$, $^\bullet OH$, $O_2^{\bullet-}$, and nonradical oxidation pathways with $^1O_2$ [19,76]. To identify the relative contribution of these various reactive species in the FeN₄/PMS system, quenching experiments were conducted during the oxidation of AO7. Experimentally, TBA, EtOH, p-benzoquinone, and L-histidine were used as selective quenchers for $^\bullet OH$, $SO_4^{\bullet-}$, $O_2^{\bullet-}$, and $^1O_2$, respectively [45]. As shown in Fig. 7a and inset, the addition of 0.1 and 0.5 M TBA into the solution decreased the degradation efficiency of AO7 only slightly from 100% to 96.9% and 91.2%, respectively, and the corresponding degradation reaction rate was reduced from 0.811 min^{-1} to 0.604 and 0.557 min^{-1}. Similarly, the catalytic degradation of AO7 was not significantly inhibited by the addition of 0.1 and 0.5 M EtOH or p-benzoquinone. These results demonstrated limited contributions from $^\bullet OH$, $SO_4^{\bullet-}$, and $O_2^{\bullet-}$ to AO7 degradation. In contrast, the AO7 degradation efficiency decreased markedly from 99.7% to 16.5% upon the addition of 0.1 M L-histidine, with an abrupt diminishment of the corresponding degradation rate from 0.811 to 0.046 min^{-1}, indicating the dominant contribution of $^1O_2$ to the degradation of AO7 by the FeN₄/PMS system.

Consistent results were obtained in EPR measurements with DMPO and TEMP as the spin-trapping agents [49]. From Fig. 7b, the signals of DMPO-SO₄ and DMPO-OH were readily detected with the FeN₄/PMS system, confirming the formation of $SO_4^{\bullet-}$ and $^\bullet OH$ radicals. In addition, a sextet characteristic of DMPO-OOH was observed in Fig. 7c, due to the generation of $O_2^{\bullet-}$. Note that the signals of $^\bullet OH$, $SO_4^{\bullet-}$, and $O_2^{\bullet-}$ were all relatively weak, suggesting that these radical species did not play a significant role in degrading AO7, in good agreement with results from the quenching experiments (Fig. 7a) [77,78]. By contrast, a strong triplet with an intensity ratio of 1:1:1, characteristic of TEMP-$^1O_2$, were observed upon the addition of TEMP (Fig. 7d), confirming the ready generation of $^1O_2$ in the FeN₄/PMS system. Additionally, the signal intensity of the TEMP-$^1O_2$ adducts was obviously higher than that of MIL-101/PMS, signifying the important role of FeN₄ moieties in facilitating

the generation of $^1O_2$. Taken together, these results suggest that the nonradical pathway ($^1O_2$) played a dominant role in AO7 degradation, with minor contributions from the radical pathways involving $^\bullet OH$, $SO_4^{\bullet-}$, and $O_2^{\bullet-}$. Similar results have been obtained in carbon/PMS systems where $^1O_2$ was found to exhibit selective degradation towards organic pollutants with electron-donating groups [30,79].

Based on these results, the mechanism of PMS activation for AO7 degradation is shown in Fig. 8. Note that $SO_4^{\bullet-}$ and $^\bullet OH$ are typically generated in a series of reactions involving the loss of Fe by electron transfer between Fe^0 and PMS (eqs. 3–6) [80], where the produced Fe^{3+} reacts with H_2O_2 (produced by oxygen reduction) to generate $HO_2^\bullet$, which is further decomposed into $O_2^{\bullet-}$ (eqs. 3–7). However, in the present study, the FeN₄ moieties were firmly embedded within the carbon skeletons, only a trace amount of Fe^0 was released into the solution, hence producing a low concentration of the radicals. This most likely accounts for their minor contributions to PMS activation.
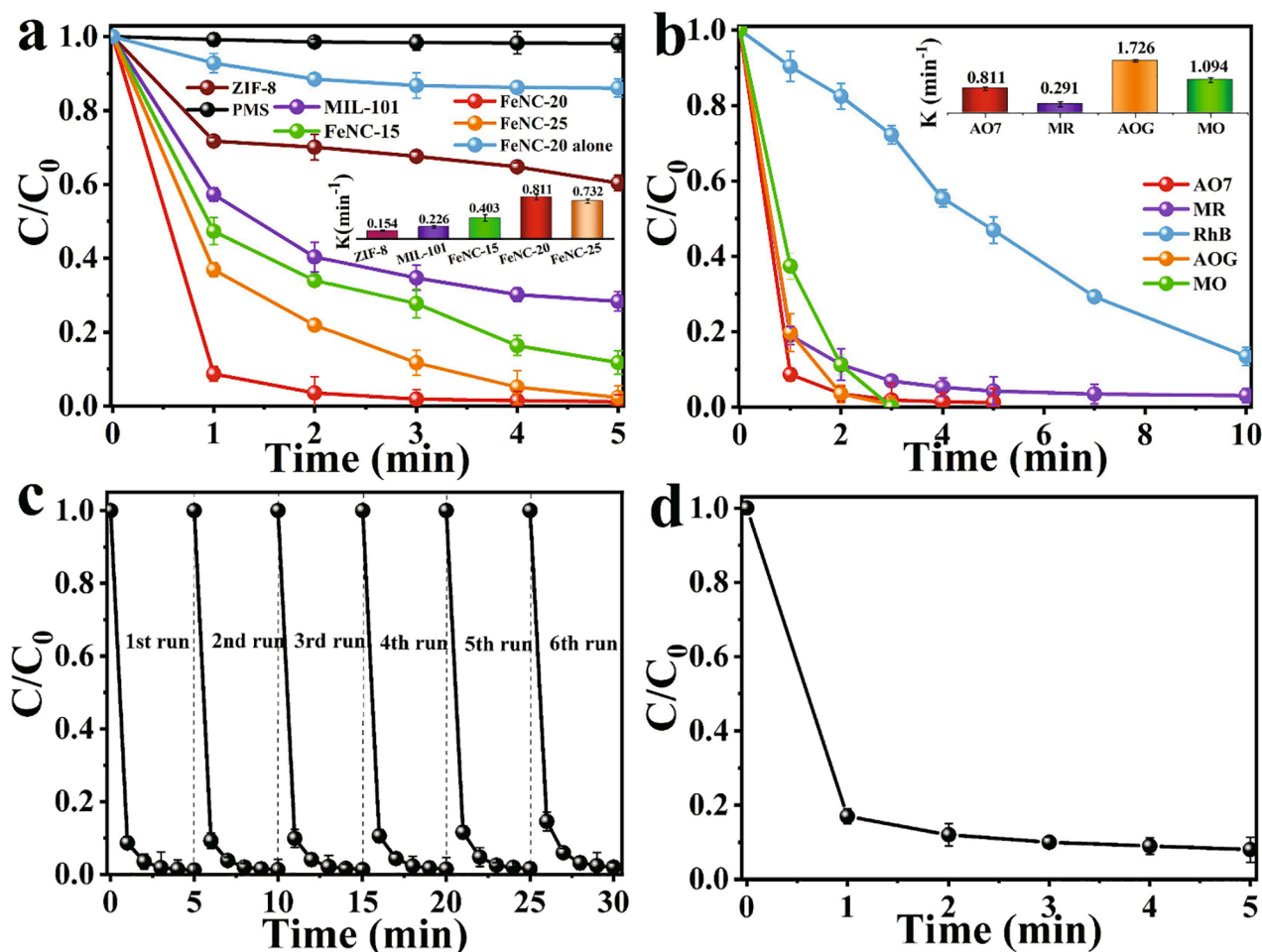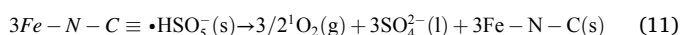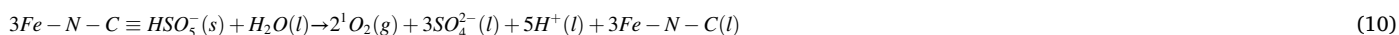
$$Fe^0(s) + 2HSO_5^-(l) \rightarrow Fe^{2+}(l) + 2SO_4^{\bullet-}(l) + 2OH^-(l) \tag{3}$$

$$Fe^{2+}(l) + HSO_5^-(l) \rightarrow Fe^{3+}(l) + SO_4^{\bullet-}(l) + OH^-(l) \tag{4}$$

$$Fe^0(s) + O_2(g) + 2H^+(l) \rightarrow Fe^{2+}(l) + H_2O_2(l) \rightarrow Fe^{3+}(l) + OH^-(l) + {}^\bullet OH(l) \tag{5}$$

$$Fe^{3+}(l) + H_2O_2(l) \rightarrow Fe^{2+}(l) + HO_2^\bullet(l) + H^+(l) \tag{6}$$

$$HO_2^\bullet(l) \rightarrow O_2^{\bullet-}(l) + H^+(l) \tag{7}$$

$$HSO_5^-(l) + SO_5^{2-}(l) \rightarrow HSO_4^-(l) + SO_4^{2-}(l) + 1O_2(g) \tag{8}$$

$$Fe - N - C(s) + HSO_5^-(l) \rightarrow Fe - N - C \equiv HSO_5^-(s) \tag{9}$$

Fig. 6. Degradation properties of AO7 in different environmental conditions. (a) Degradation of AO7 by PMS with various catalysts. (b) Degradation of various organic dyes by FeN$_C$-20 and PMS. (c) Reusability of the FeNC-20 catalyst for the degradation of AO7. (d) Variation of total organic carbon (TOC) with time. Conditions: dye concentration 50 mg L^{-1}, catalyst concentration 2 mg L^{-1}.

$$3Fe-N-C \equiv HSO_5^-(s) + H_2O(l) \rightarrow 2^1O_2(g) + 3SO_4^{2-}(l) + 5H^+(l) + 3Fe-N-C(l) \tag{10}$$

$$3Fe-N-C \equiv \bullet HSO_5^-(s) \rightarrow 3/2^1O_2(g) + 3SO_4^{2-}(l) + 3Fe-N-C(s) \tag{11}$$

It has been shown that $^1O_2$ can be produced by the self-decomposition of PMS at a rate constant of 0.2 M^{-1} s^{-1} (eq. (8)) [45]. However, the low catalytic activity of PMS alone (Fig. 6a) suggests that such a low yield of $^1O_2$ cannot be responsible for the markedly enhanced degradation performance observed with the FeNC composites. Note that production of $^1O_2$ can be readily facilitated by the formation of the unique active structure of Fe-N-C$\equiv$HSO$_5^-$ (eq. 9). Here, the Fe-N moiety serves as the active site to produce oxygen intermediates, where the N atom in FeN$_4$ extracts electrons from adjacent C atoms, and the positively charged C atoms boost the production of $^1O_2$ (eqs. 9–10). The release of $^1O_2$ from the catalyst surface can also enhance the availability of $^1O_2$ by decreasing the migration distance of the active species [81]. This is consistent with the experimental observation that the degradation efficiency of AO7 was significantly enhanced in the FeN$_4$/PMS system, as compared to that in ZIF-8 or MIL-101/PMS (Fig. 6a).

3.4. Degradation pathway

To explore the degradation pathways of AO7, the active sites of the AO7 molecule need to be identified. As $^1O_2$, an electrophilic oxidant, is the major ROS for degrading AO7 by the FeN$_4$/PMS catalyst (Fig. 7), it will most likely attack the electron-rich atomic sites in AO7 [48]. From the optimized structure of the AO7 molecule (Fig. 9a), the Fukui index (*f*) was calculated at varied atomic sites and listed in Table S6. It can be seen that 13C exhibited the highest *f* value of 0.057, and is therefore the most vulnerable site that may be attacked by $^1O_2$ in the AO7 molecule, leading to the cleavage of the C-N bond. Other atomic sites, such as 22C (0.054), 24C (0.047), 15C (0.046), 6C (0.045), 21C (0.044), and 29O (0.049), also exhibited a rather high *f* value and may serve as the attack sites, too.

In addition, the energies of the lowest unoccupied molecular orbital (LUMO) and highest occupied molecular orbital (HOMO) are calculated and shown in Fig. 9a. The red and green represent the electron-rich and -poor regions of the AO7 molecule. One can see that the HOMO mainly resides on the benzene, and electrons can be easily lost from the nitrogen atoms in AO7 molecule, leading to ring opening upon the attack of electrophilic species like $^1O_2$, O$_2^{\bullet-}$, and h$^+$. Meanwhile, the carbon
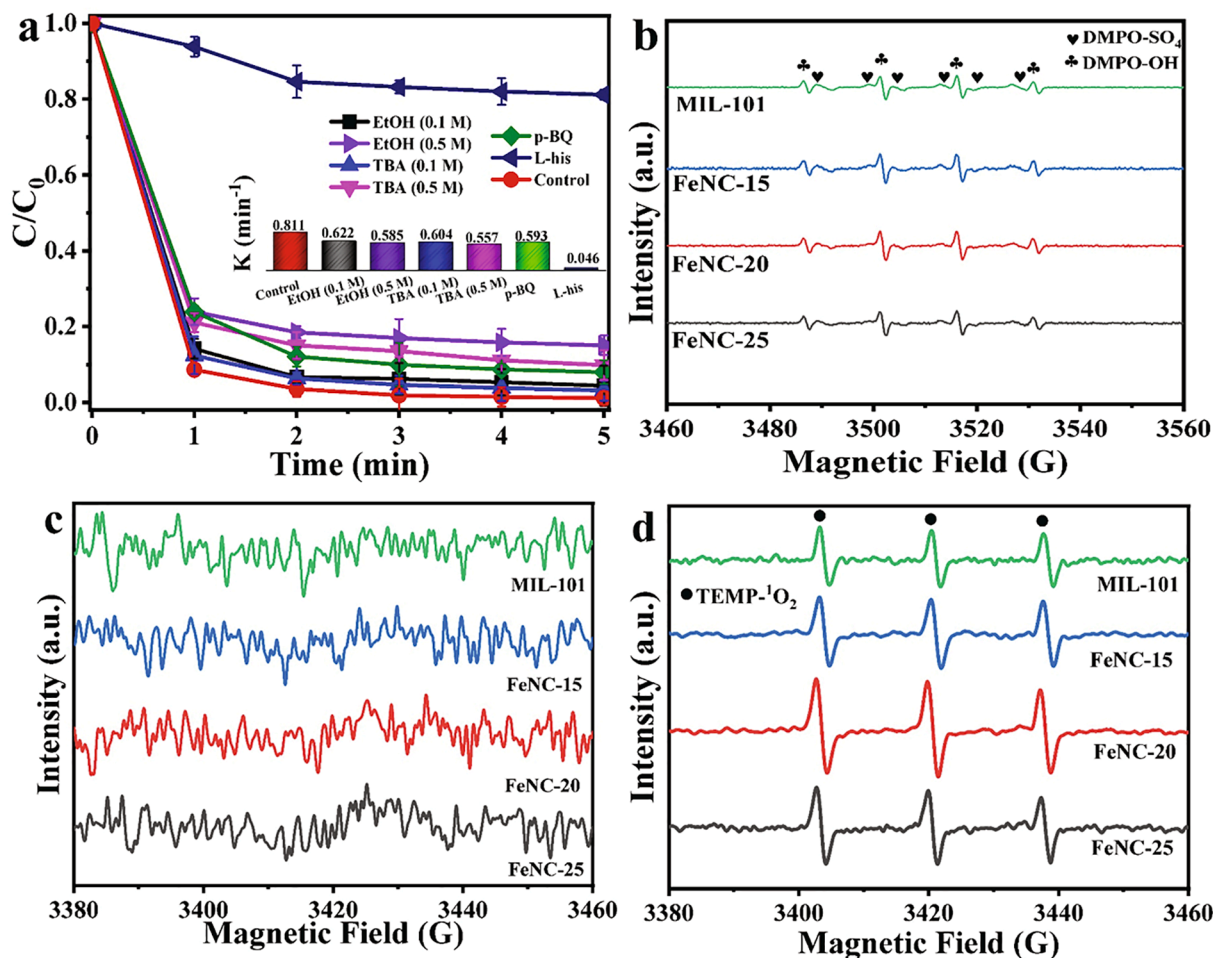
Fig. 7. (a)Effects of different quenchers on PMS activation for AO7 degradation. Inset shows the corresponding degradation reaction rate. (b) EPR spectra of DMPO-SO$_4$, DMPO-OH, (c) DMPO-OOH, and (d) TEMP-^{1}O$_2$ adduct formed after 1 min in the FeN$_4$/PMS system. Conditions: [AO7]$_0$ = 50 mg/L, [FeNC-20]$_0$ = 2 mg/L, [PMS]$_0$ = 0.5 mM/L, pH = 7.
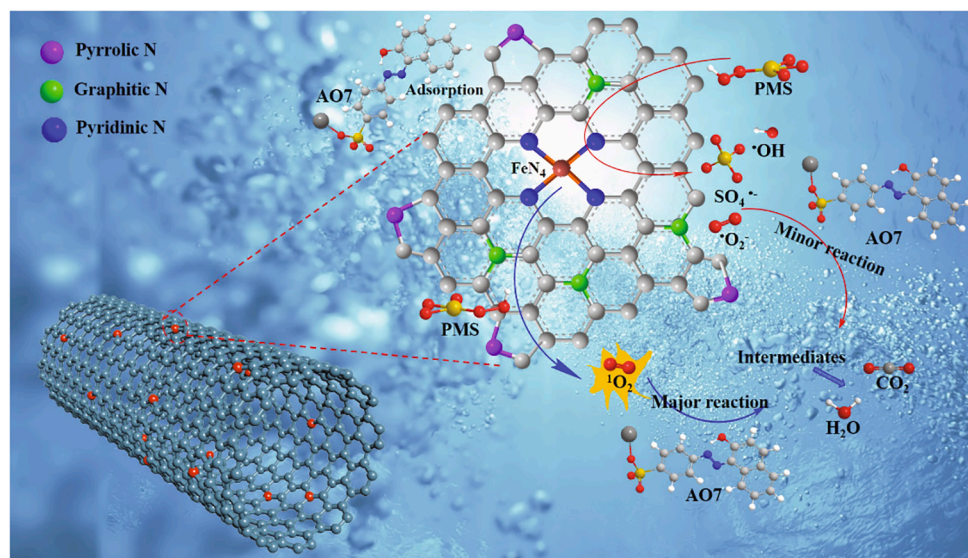

Fig. 8. Proposed reaction mechanism of AO7 degradation by the FeN$_4$/PMS system.

atoms in AO7 can be attacked by nucleophilic species as good electron acceptors [59,82,83]. In conjunction with GC–MS studies where the reaction intermediates and products were identified (Figure S16), the degradation pathway of AO7 is proposed in Fig. 9b, which starts with the breaking of the -C-N = bond between 13C and 12 N atoms due to the highest *f* value of 0.057 [84]. Meanwhile, C15 in aromatic rings was
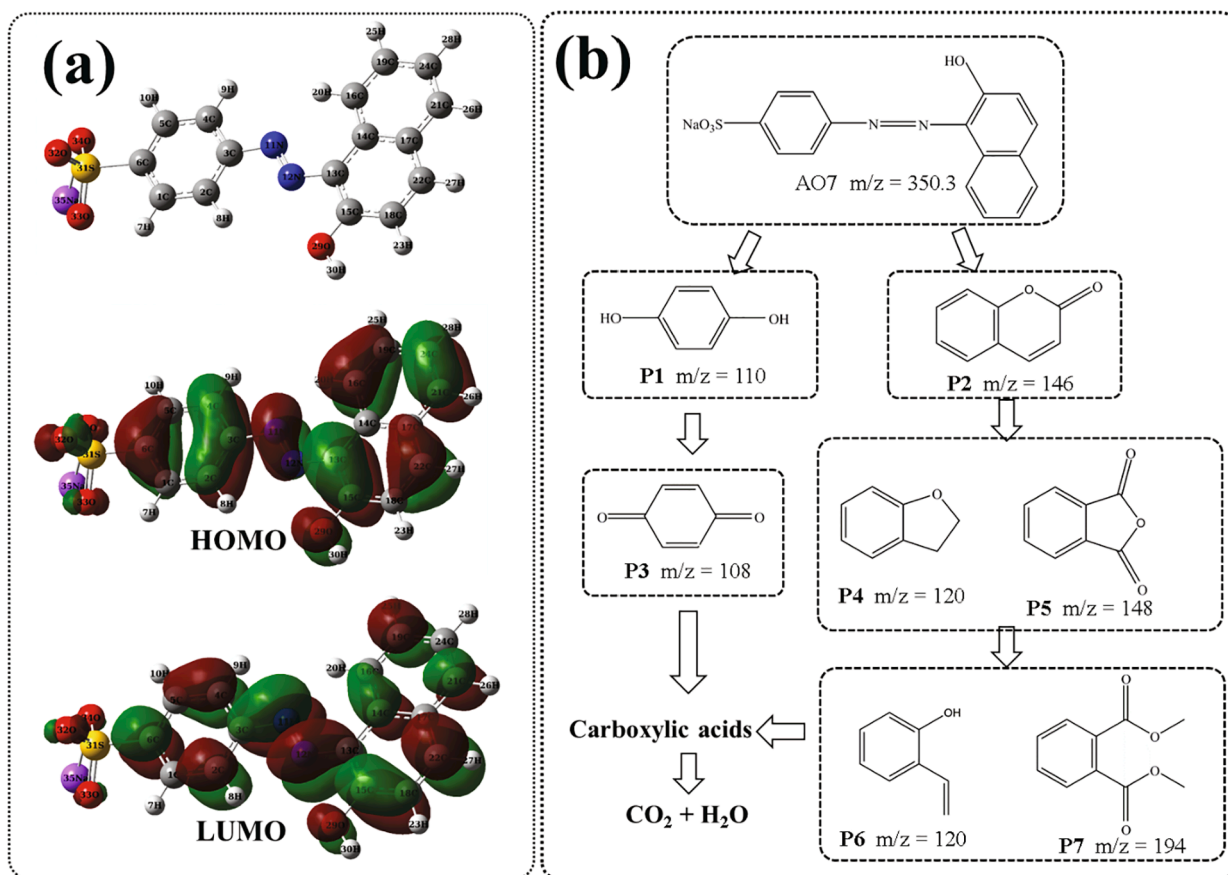
Fig. 9. (a) Optimized structure of AO7 and energies of HOMO and LUMO; the possible degradation pathways of AO7 in FeN_4/PMS system.

replaced by oxygen due to the strong attacking effect of $^1O_2$, forming a new product of $C_9H_7O_2$ (Figure S16) which was unstable and easily oxidized into P2 (m/z-146 $[M + H]^+$) due to the high redox potential of $^1O_2$ (Figure S17). In addition, based on the electrostatic potential (ESP) distribution on the $C_9H_7O_2$ molecule surface (Figure S18), it can be seen from that the region surrounding of 16O likely attracted $^1O_2$, and thus boosted the reaction. P1 is then further decomposed to P3 (m/z-108 $[M + H]^+$), and P3 is mineralized to small-molecule carboxylic acids and eventually H_2O and CO_2. Meanwhile, P2 is transformed to P4 (m/z-120 $[M + H]^+$) and P5 (m/z-148 $[M + H]^+$), due to the high charge distribution of C15 (0.046). P4 and P5 are further degraded to P6 (m/z-120 $[M + H]^+$) and P7 (m/z-194 $[M + H]^+$) by ring opening of the heterocycle moiety. Further cleavage of the aromatic rings gave rise to the generation of carboxylic acids and finally to H_2O and CO_2.

3.5. Stability and reusability of FeNC catalysts

The stability and reusability of the FeN_4/PMS catalysts was then tested by repeating the operation of AO7 degradation under the same conditions for six times, where a removal rate of 97.1% can still be achieved in 5 min (Fig. 6c), indicating a robust structure of the FeN_4/PMS catalyst. In addition, the total organic carbon (TOC) of the solution was also measured to evaluate the mineralization efficiency of FeNC-20/PMS. From Fig. 6d, one can see that the final TOC removal efficiency was ca. 92%, much higher than those of N-doped graphene and kaolinite [30,85]. Such a high mineralization efficiency was likely due to the scavenging effect for reactive oxygen species.

Furthermore, the FeNC-20 catalyst after reaction was collected by filtration and some material characterizations were carried out. The XRD patterns of the materials before and after reaction have good coincidence (Figure S19a), which proves that the materials have not

undergone phase transformation. The ratio of micropores and specific surface area did not decrease significantly (Figure S19b-19c), indicating that the skeleton structure of the material was maintained well. In Figure S19d-19f, it is obvious that the tubular structure of FeNC-20 also remains good. The XPS survey spectra revealed the changes of FeNC-20 after the degradation reaction (Figure S20). The enhancement of O peak and the appearance of S peak indicated the presence of some sulfate impurities and the increase of oxygen content in the catalyst. The high-resolution scan of the Fe 2p exhibits an increase in Fe^{3+} content (Figure S20b), which proves that Fe^{3+} is an important intermediate in the degradation of organic pollutants. This result verified the mechanism of PMS activation for AO7 degradation described above again. In addition, there is almost no change in C 1 s spectrum indicates the stability of the catalyst carbon skeleton (Figure S20c). It is worth mentioning that the relative content of FeNx (the active site) in N spectrum increases, which confirms the excellent stability of the material in catalytic degradation reaction.

4. Conclusions

In summary, carbon nanotubes embedded with FeN_4 moieties were successfully prepared by a ball milling and pyrolysis method and exhibited unique activity in the activation of PMS for effective degradation of a range of organic pollutants. Spectroscopic measurements suggest that the degradation reaction occurred primarily via the non-radical pathway involving $^1O_2$ singlet oxygen, with minor contributions from the radical pathways involving $^{\bullet}OH$, $SO_4^{\bullet-}$, and $O_2^{\bullet-}$. DFT calculations revealed that the spin property of the FeN_4 moieties played a critical role in PMS adsorption and activation, and low- and medium-spin FeN_4 was the most active species for the generation of $^1O_2$. Results from this study highlight the significance of carbon-supported

single atom catalysts in the degradation of organic pollutants, a key step towards environmental remediation.

Declaration of Competing Interest

The authors declare that they have no known competing financial interests or personal relationships that could have appeared to influence the work reported in this paper.

Acknowledgement

Appendix A. Supplementary data

Supplementary data to this article can be found online at https://doi.org/10.1016/j.cej.2021.133339.

References

[1] Y. Leng, J. Bao, D. Song, J. Li, M. Ye, X.u. Li, Background Nutrients Affect the Biotransformation of Tetracycline by Stenotrophomonas maltophilia as Revealed by Genomics and Proteomics, Environ. Sci. Technol. 51 (18) (2017) 10476–10484.

[2] M.M. Mian, G. Liu, B. Fu, Y. Song, Facile synthesis of sludge-derived MnOx-N-biochar as an efficient catalyst for peroxymonosulfate activation, Appl. Catal. B-Environ. 255 (2019), 117765.

[3] E. Borowska, E. Felis, J. Kalka, Oxidation of benzotriazole and benzothiazole in photochemical processes: Kinetics and formation of transformation products, Chem. Eng. J. 304 (2016) 852–863.

[4] S. Deng, L. Jothinathan, Q. Cai, R. Li, M. Wu, S.L. Ong, J. Hu, FeOx@GAC catalyzed microbubble ozonation coupled with biological process for industrial phenolic wastewater treatment: Catalytic performance, biological process screening and microbial characteristics, water Res. 190 (2021), 116687.

[5] Y. Qiu, Y. Xu, Z. Xu, J. Liang, Y. Yu, X. Cao, Contribution of different iron species in the iron-biochar composites to sorption and degradation of two dyes with varying properties, Chem. Eng. J. 389 (2020), 124471.

[6] A.A. Mohammed, M.A. Atiya, M.A. Hussein, Simultaneous studies of emulsion stability and extraction capacity for the removal of tetracycline from aqueous solution by liquid surfactant membrane, Chem. Eng. J. 159 (2020) 225–235.

[7] Y. Liu, Y. Zhao, J. Wang, Fenton/Fenton-like processes with in-situ production of hydrogen peroxide/hydroxyl radical for degradation of emerging contaminants: Advances and prospects, J. Hazard. Mater. 404 (2021) 124191, https://doi.org/10.1016/j.jhazmat.2020.124191.

[8] P. Sun, T. Meng, Z. Wang, R. Zhang, H. Yao, Y. Yang, L. Zhao, Degradation of Organic Micropollutants in UV/NH2Cl Advanced Oxidation Process, Environ. Sci. Technol. 53 (15) (2019) 9024–9033.

[9] L. Hou, X. Li, Q. Yang, F. Chen, S. Wang, Y. Ma, Y. Wu, X. Zhu, X. Huang, D. Wang, Heterogeneous activation of peroxymonosulfate using Mn-Fe layered double hydroxide: Performance and mechanism for organic pollutant degradation, Sci. Total Environ. 663 (2019) 453–464.

[10] B.C. Huang, J. Jiang, G.X. Huang, H.Q. Yu, Sludge biochar-based catalysts for improved pollutant degradation by activating peroxymonosulfate, J. Mater. Chem. A 6 (2018) 89788985.

[11] W. Ma, Y. Du, N.a. Wang, P. Miao, ZIF-8 derived nitrogen-doped porous carbon as metal-free catalyst of peroxymonosulfate activation, Environ. Sci. Pollut. Res. 24 (19) (2017) 16276–16288.

[12] X. Huang, X. Zhou, J. Zhou, Z. Huang, S. Liu, G. Qian, N. Gao, Bromate inhibition by reduced graphene oxide in thermal/PMS process, Water Res. 122 (2017) 701–707.

[13] K.Z. Huang, H.C. Zhang, Direct Electron-Transfer-Based Peroxymonosulfate Activation by Iron-Doped Manganese Oxide (delta-MnO2) and the Development of Galvanic Oxidation Processes (GOPs), Environ. Sci. Technol. 53 (2019) 12610–12620.

[14] Y. Huang, C. Han, Y. Liu, M.N. Nadagouda, L. Machala, K.E. O'Shea, V.K. Sharma, D.D. Dionysiou, Degradation of atrazine by ZnxCu1−xFe2O4 nanomaterial

[15] D. Miao, S. Zhao, K. Zhu, P. Zhang, T. Wang, H. Jia, H. Sun, Activation of persulfate and removal of ethyl-parathion from soil: Effect of microwave irradiation, Chemosphere 253 (2020), 126679.

[16] X. Li, Y. Jia, M. Zhou, X. Su, J. Sun, High-efficiency degradation of organic pollutants with Fe, N co-doped biochar catalysts via persulfate activation, J. Hazard. Mater. 397 (2020), 122764.

[17] S. Wang, Y. Liu, J. Wang, Peroxymonosulfate Activation by Fe-Co-O-Codoped Graphite Carbon Nitride for Degradation of Sulfamethoxazole, Environ. Sci. Technol. 54 (16) (2020) 10361–10369.

[18] X. Duan, C. Su, J. Miao, Y. Zhong, Z. Shao, S. Wang, H. Sun, Insights into perovskite-catalyzed peroxymonosulfate activation: Maneuverable cobalt sites for promoted evolution of sulfate radicals, Appl. Catal. B-Environ. 220 (2018) 626–634.

[19] W. Ren, L. Xiong, X. Yuan, Z. Yu, H. Zhang, X. Duan, S. Wang, Activation of Peroxydisulfate on Carbon Nanotubes: Electron-Transfer Mechanism, Environ. Sci. Technol. 53 (2019) 14595–14603.

[20] M. Li, Y. Li, P. Yu, H. Zhao, L. Xiang, N. Feng, Q. Li, K. He, X. Luo, Q. Cai, S. Zhou, C. Mo, K. Yeung, Exploring degradation mechanism of tetracycline via high-effective peroxymonosulfate catalysts of montmorillonite hybridized CoFe composites and safety assessment, Chem. Eng. J. 427 (2022), 130930.

[21] Y. Feng, P.-H. Lee, D. Wu, K. Shih, Rapid Selective Circumneutral Degradation of Phenolic Pollutants Using Peroxymonosulfate-Iodide Metal-Free Oxidation: Role of Iodine Atoms, Environ. Sci. Technol. 51 (4) (2017) 2312–2320.

[22] E.T. Yun, J.H. Lee, J. Kim, H.D. Park, J. Lee, Identifying the nonradical mechanism in the peroxymonosulfate activation process: Singlet oxygenation versus mediated electron transfer, Environ. Sci. Technol. 52 (2018) 7032–7042.

[23] J. Zhang, X. Shao, C. Shi, S. Yang, Decolorization of Acid Orange 7 with peroxymonosulfate oxidation catalyzed by granular activated carbon, Chem. Eng. J. 232 (2013) 259–265.

[24] S. Wang, J. Wang, Kinetics of PMS activation by graphene oxide and biochar, Chemosphere 239 (2019), 124812.

[25] J. Wang, X. Duan, J. Gao, Y. Sheng, S. Wang, Roles of structure defect, oxygen groups and heteroatom doping on carbon in nonradical oxidation of water contaminants, Water Res. 185 (2020), 116244.

[26] H. Lee, H.-i. Kim, S. Weon, W. Choi, Y.S. Hwang, J. Seo, C. Lee, J.-H. Kim, Activation of Persulfates by Graphitized Nanodiamonds for Removal of Organic Compounds, Environ. Sci. Technol. 50 (18) (2016) 10134–10142.

[27] I. Pikaar, K.R. Sharma, S. Hu, W. Gernjak, J. Keller, Z. Yuan, Reducing sewer corrosion through integrated urban water management, Science 345 (6198) (2014) 812–814.

[28] D. Guo, R. Shibuya, C. Akiba, S. Saji, T. Kondo, J. Nakamura, Active sites of nitrogen-doped carbon materials for oxygen reduction reaction clarified using model catalysts, Science 351 (6271) (2016) 361–365.

[29] L.Z.Z. Liu, L. Sheng, Q. Zhou, T. Wei, J. Feng, Z. Fan, Edge-nitrogen-rich carbon dots pillared graphene blocks with ultrahigh volumetric/gravimetric capacities and ultralong life for sodium-ion storage, Adv. Energy Mater. 8 (2018) 1802042.

[30] P. Sun, H. Liu, M. Feng, L. Guo, Z. Zhai, Y. Fang, X. Zhang, V.K. Sharma, Nitrogen-sulfur co-doped industrial graphene as an efficient peroxymonosulfate activator: Singlet oxygen-dominated catalytic degradation of organic contaminants, Appl. Catal. B-Environ. 251 (2019) 335–345.

[31] S.-H. Ho, Y.-d. Chen, R. Li, C. Zhang, Y. Ge, G. Cao, M. Ma, X. Duan, S. Wang, N.-q. Ren, N-doped graphitic biochars from C-phycocyanin extracted Spirulina residue for catalytic persulfate activation toward nonradical disinfection and organic oxidation, Water Res. 159 (2019) 77–86.

[32] X. Duan, H. Sun, Y. Wang, J. Kang, S. Wang, N-doping-induced nonradical reaction on single-walled carbon nanotubes for catalytic phenol oxidation, ACS Catal. 5 (2) (2015) 553–559.

[33] W. Sang, Z. Li, M. Huang, X. Wu, D. Li, L. Mei, J. Cui, Enhanced transition metal oxide based peroxymonosulfate activation by hydroxylamine for the degradation of sulfamethoxazole, Chem. Eng. J. 383 (2020), 123057.

[34] Y.-C. Wang, Y.-J. Lai, L. Song, Z.-Y. Zhou, J.-G. Liu, Q. Wang, X.-D. Yang, C. Chen, W. Shi, Y.-P. Zheng, M. Rauf, S.-G. Sun, S-doping of an Fe/N/C ORR catalyst for polymer electrolyte membrane fuel cells with high power density, Angew. Chem. Int. Edit. 54 (34) (2015) 9907–9910.

[35] Y. Long, Y. Huang, H. Wu, X. Shi, L. Xiao, Peroxymonosulfate activation for pollutants degradation by Fe-N-codoped carbonaceous catalyst: Structure-dependent performance and mechanism insight, Chem. Eng. J. 369 (2019) 542–552.

[36] W. Ma, N.a. Wang, Y. Du, T. Tong, L. Zhang, K.-Y. Andrew Lin, X. Han, One-step synthesis of novel Fe3C@nitrogen-doped carbon nanotubes/graphene nanosheets for catalytic degradation of Bisphenol A in the presence of peroxymonosulfate, Chem. Eng. J. 356 (2019) 1022–1031.

[37] Y.J. Sa, D.-J. Seo, J. Woo, J.T. Lim, J.Y. Cheon, S.Y. Yang, J.M. Lee, D. Kang, T. J. Shin, H.S. Shin, H.Y. Jeong, C.S. Kim, M.G. Kim, T.-Y. Kim, S.H. Joo, A general approach to preferential formation of active Fe-Nx sites in Fe-N/C electrocatalysts for efficient oxygen reduction reaction, J. Am. Chem. Soc. 138 (45) (2016) 15046–15056.

[38] R. Jiang, L.i. Li, T. Sheng, G. Hu, Y. Chen, L. Wang, Edge-site engineering of atomically dispersed Fe-N4 by selective C-N bond cleavage for enhanced oxygen reduction reaction activities, J. Am. Chem. Soc. 140 (37) (2018) 11594–11598.

[39] Y. Liu, W. Miao, X. Fang, Y.L. Tang, D.L. Wu, S. Mao, MOF-derived metal-free N doped porous carbon mediated peroxydisulfate activation via radical and nonradical pathways: role of graphitic N and C-O, Chem. Eng. J. 380 (2020), 122584.

[40] X. Li, X. Huang, S. Xi, S. Miao, J. Ding, W. Cai, S. Liu, X. Yang, H. Yang, J. Gao, J. Wang, Y. Huang, T. Zhang, B. Liu, Single cobalt atoms anchored on porous N doped graphene with dual reaction sites for efficient fenton-like catalysis, J. Am. Chem. Soc. 140 (39) (2018) 12469–12475.

[41] X. Wan, W. Chen, J. Yang, M. Liu, X. Liu, J. Shui, Synthesis and active site identification of Fe−N−C single-atom catalysts for the oxygen reduction reaction, ChemElectroChem 6 (2) (2019) 304–315.

[42] H. Zhang, S. Hwang, M. Wang, Z. Feng, S. Karakalos, L. Luo, Z. Qiao, X. Xie, C. Wang, D. Su, Y. Shao, G. Wu, Single atomic iron catalysts for oxygen reduction in acidic media: particle size control and thermal activation, J. Am. Chem. Soc. 139 (2017) 14143–14149.

[43] F.-M. Zhang, L.-Z. Dong, J.-S. Qin, W. Guan, J. Liu, S.-L. Li, M. Lu, Y.-Q. Lan, Z.-M. Su, H.-C. Zhou, Effect of Imidazole Arrangements on Proton-Conductivity in Metal-Organic Frameworks, J. Am. Chem. Soc. 139 (17) (2017) 6183–6189.

[44] Z. Zeng, S. Fang, W. Miao, Y. Liu, T. Maiyalagan, S. Mao, Electrochemically sensing of trichloroacetic acid with iron(II) phthalocyanine and Zn-based metal organic framework nanocomposites, ACS Sensors 4 (7) (2019) 1934–1941.

[45] P. Liang, C. Zhang, X. Duan, H. Sun, S. Liu, M.O. Tade, S. Wang, An insight into metal organic framework derived N-doped graphene for the oxidative degradation of persistent contaminants: formation mechanism and generation of singlet oxygen from peroxymonosulfate, Environ. Sci.-Nano 4 (2017) 315–324.

[46] L. Gao, M. Xiao, Z. Jin, C. Liu, J. Zhu, J. Ge, W. Xing, Correlating Fe source with Fe-N-C active site construction: Guidance for rational design of high-performance ORR catalyst, J. Energy Chem. 27 (2018) 1668–1673.

[47] Y. Chen, S. Ji, Y. Wang, J. Dong, W. Chen, Z. Li, R. Shen, L. Zheng, Z. Zhuang, D. Wang, Y. Li, Isolated single iron atoms anchored on N-doped porous carbon as an efficient electrocatalyst for the oxygen reduction reaction, Angew. Chem. Int. Ed. Engl. 56 (24) (2017) 6937–6941.

[48] Y. Gao, Y. Zhu, L. Lyu, Q. Zeng, X. Xing, C. Hu, Electronic structure modulation of graphitic carbon nitride by oxygen doping for enhanced catalytic degradation of organic pollutants through peroxymonosulfate activation, Environ. Sci. Technol. 52 (24) (2018) 14371–14380.

[49] S. Wu, H. Liu, C. Yang, X. Li, Y. Lin, K. Yin, J. Sun, Q. Teng, C. Du, Y. Zhong, High-performance porous carbon catalysts doped by iron and nitrogen for degradation of bisphenol F via peroxymonosulfate activation, Chem. Eng. J. 392 (2020), 123683.

[50] Y. Li, T. Yang, S. Qiu, W. Lin, J. Yan, S. Fan, Q. Zhou, Uniform N-coordinated single-atomic iron sites dispersed in porous carbon framework to activate PMS for efficient BPA degradation via high-valent iron-oxo species, Chem. Eng. J. 389 (2020), 124382.

[51] P. Gao, X. Tian, W. Fu, Y. Wang, Y. Nie, C. Yang, Y. Deng, Copper in LaMnO3 to promote peroxymonosulfate activation by regulating the reactive oxygen species in sulfamethoxazole degradation, J. Hazard. Mater. 411 (2021), 125163.

[52] X. Zhao, Q.-D. An, Z.-Y. Xiao, S.-R. Zhai, Z. Shi, Seaweed-derived multifunctional nitrogen/cobalt-codoped carbonaceous beads for relatively high-efficient peroxymonosulfate activation for organic pollutants degradation, Chem. Eng. J. 353 (2018) 746–759.

[53] Y. Liu, X. Chen, Y. Yang, Y. Feng, D. Wu, S. Mao, Activation of persulfate with metal–organic framework-derived nitrogen-doped porous Co@C nanoboxes for highly efficient p-Chloroaniline removal, Chem. Eng. J. 358 (2019) 408–418.

[54] W. Ma, N.a. Wang, Y. Fan, T. Tong, X. Han, Y. Du, Non-radical-dominated catalytic degradation of bisphenol A by ZIF-67 derived nitrogen-doped carbon nanotubes frameworks in the presence of peroxymonosulfate, Chem. Eng. J. 336 (2018) 721–731.

[55] Q. Lai, L. Zheng, Y. Liang, J. He, J. Zhao, J. Chen, Metal–Organic-Framework-Derived Fe-N/C Electrocatalyst with Five-Coordinated Fe-Nx Sites for Advanced Oxygen Reduction in Acid Media, ACS Catalysis 7 (3) (2017) 1655–1663.

[56] H. Hu, H. Zhang, Y. Chen, Y. Chen, L. Zhuang, H. Ou, Enhanced photocatalysis degradation of organophosphorus flame retardant using MIL-101(Fe)/persulfate: Effect of irradiation wavelength and real water matrixes, Chem. Eng. J. 368 (2019) 273–284.

[57] B.Y. Guan, L.e. Yu, X.W. (David) Lou, A dual-metal–organic-framework derived electrocatalyst for oxygen reduction, Energy Environ. Sci. 9 (10) (2016) 3092–3096.

[58] C. Zhao, J. Wang, X. Chen, Z. Wang, H. Ji, L. Chen, W. Liu, C.C. Wang, Bifunctional Bi12O17Cl2/MIL-100(Fe) composites toward photocatalytic Cr(VI) sequestration and activation of persulfate for bisphenol A degradation, Sci. Total. Environ. 752 (2021) 141901.

[59] X.-H. Yi, H. Ji, C.-C. Wang, Y. Li, Y.-H. Li, C. Zhao, A. Wang, H. Fu, P. Wang, X. Zhao, W. Liu, Photocatalysis-activated SR-AOP over PDINH/MIL-88A(Fe) composites for boosted chloroquine phosphate degradation: Performance, mechanism, pathway and DFT calculations, Applied Catalysis B: Environmental 293 (2021), 120229.

[60] W. Du, Q. Zhang, Y. Shang, W. Wang, Q. Li, Q. Yue, B. Gao, X. Xu, Sulfate saturated biosorbent-derived Co-S@NC nanoarchitecture as an efficient catalyst for peroxymonosulfate activation, Appl. Catal. B Environ. 262 (2020) 118302, https://doi.org/10.1016/j.apcatb.2019.118302.

[61] M. Frisch, G. Trucks, H.B. Schlegel, G.E. Scuseria, M.A. Robb, J.R. Cheeseman, G. Scalmani, V. Barone, B. Mennucci, G. Petersson, Gaussian 09, Revision D. 01. Gaussian. Inc., Wallingford CT, 201 (2009).

[62] T. Lu, F.M. Chen, Multiwfn: A Multifunctional Wavefunction Analyzer, J. Comput. Chem. 33 (2012) 580–592.

[63] N. Cheng, J.C. Li, D. Liu, Y. Lin, D. Du, Single-Atom Nanozyme Based on Nanoengineered Fe–N–C Catalyst with Superior Peroxidase-Like Activity for Ultrasensitive Bioassays, Small 15 (2019) 1901485.

[64] K.S.W. Sing, R.T. Williams, Physisorption hysteresis loops and the characterization of nanoporous materials, Adsorpt. Sci. Technol. 22 (10) (2004) 773–782.

[65] F. Jaouen, M. Lefèvre, J.P. Dodelet, M. Cai, Heat-treated Fe/N/C catalysts for O2 electroreduction: Are active sites hosted in micropores? J. Phys. Chem. B. 110 (2006) 5553–5558.

[66] M.A. Pimenta, G. Dresselhaus, M.S. Dresselhaus, L.G. Cançado, A. Jorio, R. Saito, Studying disorder in graphite-based systems by Raman spectroscopy, Phys. Chem. Chem. Phys. 9 (11) (2007) 1276–1290.

[67] U.I. Kramm, M. Lefèvre, N. Larouche, D. Schmeisser, J.-P. Dodelet, Correlations between Mass Activity and Physicochemical Properties of Fe/N/C Catalysts for the ORR in PEM Fuel Cell via 57Fe Mössbauer Spectroscopy and Other Techniques, J. Am. Chem. Soc. 136 (3) (2014) 978–985.

[68] D. Xia, X. Yang, L. Xie, Y. Wei, W. Jiang, M. Dou, X. Li, J. Li, L. Gan, F. Kang, Direct Growth of Carbon Nanotubes Doped with Single Atomic Fe–N4 Active Sites and Neighboring Graphitic Nitrogen for Efficient and Stable Oxygen Reduction Electrocatalysis, Adv. Funct. Mater. 29 (2019) 1906174.

[69] U.I. Kramm, J. Herranz, N. Larouche, T.M. Arruda, M. Lefèvre, F. Jaouen, P. Bogdanoff, S. Fiechter, I. Abs-Wurmbach, S. Mukerjee, J.-P. Dodelet, Structure of the catalytic sites in Fe/N/C-catalysts for O2-reduction in PEM fuel cells, Phys. Chem. Chem. Phys. 14 (33) (2012) 11673, https://doi.org/10.1039/c2cp41957b.

[70] Y. Wu, J. Huang, Z. Lin, L. Li, G. Liang, Y. Jin, G. Huang, H. Zhang, J. Chen, F. Xie, Y. Jin, N. Wang, H. Meng, Fe-Nx doped carbon nanotube as a high efficient cathode catalyst for proton exchange membrane fuel cell, Chem. Eng. J. 423 (2021), 130241.

[71] M. Lefèvre, E. Proietti, Frédéric Jaouen, J.-P. Dodelet, Iron-based catalysts with improved oxygen reduction activity in polymer electrolyte fuel cells, Science 324 (5923) (2009) 71–74.

[72] G. Wu, K.L. More, C.M. Johnston, P. Zelenay, High-performance electrocatalysts for oxygen reduction derived from polyaniline, iron, and cobalt, Science 332 (6028) (2011) 443–447.

[73] R. Chenitz, U.I. Kramm, M. Lefèvre, V. Glibin, G. Zhang, S. Sun, J.-P. Dodelet, A specific demetalation of Fe–N 4 catalytic sites in the micropores of NC_Ar+ NH 3 is at the origin of the initial activity loss of the highly active Fe/N/C catalyst used for the reduction of oxygen in PEM fuel cells, Energy Environ. Sci. 11 (2) (2018) 365–382.

[74] Y. Zhan, F. Xie, H. Zhang, Y. Jin, H. Meng, J. Chen, X. Sun, Highly Dispersed Nonprecious Metal Catalyst for Oxygen Reduction Reaction in Proton Exchange Membrane Fuel Cells, ACS Appl. Mater. Interfaces 12 (15) (2020) 17481–17491.

[75] Y. Zhan, H. Zeng, F. Xie, H. Zhang, W. Zhang, Y. Jin, Y. Zhang, J. Chen, H. Meng, Templated growth of Fe/N/C catalyst on hierarchically porous carbon for oxygen reduction reaction in proton exchange membrane fuel cells, J. Power Sources 431 (2019) 31–39.

[76] W. Ren, G. Nie, P. Zhou, H. Zhang, X. Duan, S. Wang, The Intrinsic Nature of Persulfate Activation and N-Doping in Carbocatalysis, Environ. Sci. Technol. 54 (10) (2020) 6438–6447.

[77] P. Liang, C. Zhang, X. Duan, H. Sun, S. Liu, M.O. Tade, S. Wang, N-doped graphene from metal organic frameworks for catalytic oxidation of p-hydroxylbenzoic acid: N functionality and mechanism, ACS Sustain. Chem. Eng. 5 (3) (2017) 2693–2701.

[78] B. Shao, H. Dong, B.o. Sun, X. Guan, Role of ferrate (IV) and ferrate (V) in activating ferrate (VI) by calcium sulfite for enhanced oxidation of organic contaminants, Environ. Sci. Technol. 53 (2) (2019) 894–902.

[79] S.S. Zhu, X.J. Li, J. Kang, X.G. Duan, S.B. Wang, Persulfate activation on crystallographic manganese oxides: mechanism of singlet oxygen evolution for nonradical selective degradation of aqueous contaminants, Environ. Sci. Technol. 53 (2019) 307–315.

[80] H.W. Liang, X. Zhuang, S. Bruller, X. Feng, K. Mullen, Hierarchically porous carbons with optimized nitrogen doping as highly active electrocatalysts for oxygen reduction, Nat. Commun. 5 (2014) 4973.

[81] L. Xu, B. Fu, Y. Sun, P. Jin, X. Bai, X. Jin, X. Shi, Y. Wang, S. Nie, Degradation of organic pollutants by Fe/N co-doped biochar via peroxymonosulfate activation: Synthesis, Performance, mechanism and its potential for practical application, Chem. Eng. J. 400 (2020) 125870.

[82] R. Xiao, Z. Luo, Z. Wei, S. Luo, R. Spinney, W. Yang, D.D. Dionysiou, Activation of peroxymonosulfate/persulfate by nanomaterials for sulfate radical-based advanced oxidation technologies, Curr. Opin. Chem. Eng. 19 (2018) 51–58.

[83] L. Chen, H. Ji, J. Qi, T. Huang, C.-C. Wang, W. Liu, Degradation of acetaminophen by activated peroxymonosulfate using Co(OH)2 hollow microsphere supported titanate nanotubes: Insights into sulfate radical production pathway through CoOH + activation, Chem. Eng. J. 406 (2021), 126877.

[84] J.H. Shen, H.Y. Chuang, Z.W. Jiang, X.Z. Liu, J.J. Horng, Novel quantification of formation trend and reaction efficiency of hydroxyl radicals for investigating photocatalytic mechanism of Fe-doped TiO2 during UV and visible light-induced degradation of acid orange 7, Chemosphere 251 (2020), 126380.

[85] C. Li, Y. Huang, X. Dong, Z. Sun, X. Duan, B. Ren, S. Zheng, D.D. Dionysiou, Highly efficient activation of peroxymonosulfate by natural negatively-charged kaolinite with abundant hydroxyl groups for the degradation of atrazine, Appl. Catal. B-Environ. 247 (2019) 10–23.